Dynamics of the Coupled Moist Kelvin–Rossby Wave on an Equatorial β-Plane*

BIN WANG AND HUALAN RUI

Department of Meteorology, University of Hawaii, Honolulu, Hawaii

(Manuscript received 6 March 1989, in final form 18 July 1989)

ABSTRACT

A simple theoretical analysis on the stability of a resting tropical atmosphere to semigeostrophic perturbations is given using a free atmosphere–boundary layer coupled model on an equatorial β-plane.

An unstable mode emerges when sea surface temperature is higher than a critical value. The growing mode is a moist Kelvin wave modified through coupling with a Rossby wave of the lowest meridional index. The modified Rossby modes, however, remain damped even for high SST. The unstable *mode selection* can be explained in terms of wave energy generation due to the latent heating induced by frictional moisture convergence.

The horizontal mode-coupling has profound impacts on wave instability. It favors the amplification of long planetary-scale waves, slows down eastward propagation, and suppresses unrealistically fast growth of the un-coupled moist Kelvin mode by creating substantial meridional flows. These effects make the coupled unstable mode more resemble observed equatorial intraseasonal disturbances.

The results also demonstrate that when maximum SST moves from the equator to 7.5°N, the growth rate of the unstable wave is significantly reduced, suggesting that the annual march of the "thermal equator" and associated convective heating is likely responsible for annual variations of the equatorial 40–50 day wave activity.

1. Introduction

The slowly eastward-moving equatorial convection and circulation anomaly first described by Madden and Julian (1972) is believed to be a dominant mode of tropical intraseasonal variations. Numerical studies demonstrate that condensational heating interacting with equatorial wave motions may maintain long-lasting transient disturbances that have a zonal scale of wavenumber 1 or 2 and move eastward at a speed of about 10–20 m s^{-1}. In many aspects the long-lasting modes found in these idealized numerical models resemble the observed intraseasonal oscillation modes. It was suggested that the intraseasonal oscillation is associated with a Kelvin wave–CISK mode (Lau and Peng 1987; Swinbank et al. 1987; Lau et al. 1988), or a coupled Kelvin–Rossby mode (Hayashi and Sumi 1986; Hendon 1988).

Attempts have been made to understand intraseasonal oscillation in terms of moist equatorial wave dynamics. A number of recent theoretical model studies have provided useful insights into moist Kelvin wave dynamics (e.g., Lau and Shen 1988; Chang and Lim

1988; Wang 1988a). Yet these analyses are confined to two-dimensional motion in the equatorial zonal plane. The present study is an extension of moist Kelvin wave analysis by using a dynamically consistent model that includes a meridional component of the motion; namely, the intrinsic modes in the model include both the eastward propagating Kelvin wave and the westward-propagating long Rossby waves.

One of the main objectives of the present study is to examine the impacts of the presence of meridional winds on moist wave dynamics. Some recent eigenmode analyses suggested that equatorial Rossby waves are stable with respect to time-lag CISK effects (Chang and Lim 1988) and are damped by evaporation–wind feedback (Neelin et al. 1987). An important question remains unclear; that is, what is responsible for this unstable mode selection? Equatorial Rossby modes appear to play important roles in moist adjustment processes in the tropics (Yamagata 1987) and in determining horizontal structure of intraseasonal disturbances (Hayashi and Sumi 1986). In the presence of boundary-layer moisture convergence, how does the presence of long Rossby modes affect the amplification, propagation, and horizontal structure of the moist unstable Kelvin mode? The examination of the effects and mechanism of the coupling between moist equatorial Kelvin and Rossby waves are expected to provide useful insight into low-frequency wave dynamics.

Another aspect to be addressed is the cause of significant seasonality of the equatorial low-frequency wave activity. By analyzing 19 near-equatorial station

---

Corresponding author address: Dr. Bin Wang, Department of Meteorology, University of Hawaii, 2525 Correa Road, Honolulu, HI 96822.

397

rawinsonde data, Madden (1986) showed that the intraseasonal variability in zonal wind exceeds that in adjacent lower and higher frequency bands by the largest amount during December, January, and February. Using ten years of outgoing longwave radiation (OLR) data, we investigated temporal variations of 77 low-frequency eastward-moving equatorial events and found that the overall intensity of intraseasonal convective anomalies are significantly stronger in boreal winter (from November to April) than in boreal summer (Wang and Rui 1989). Madden (1986) speculated on the role of convective heating distribution in annual variation of low frequency wave activities. We shall examine the relationship between SST variation and wave instability using a simple model developed in sections 2 and 3.

2. A simplified dynamic framework

Observed low frequency waves are characterized by anisotropic horizontal length scales: the zonal scale (L_x $\sim 10^7$ km) is much larger than the meridional scale ($L_y \sim 10^6$ km). A scale analysis shows that the meridional acceleration in v-momentum equation can be neglected. The zonal wind component is thus in geostrophic balance with meridional pressure gradient and the motion is semigeostrophic. With this approximation, high frequency inertio–gravity waves, mixed Rossby–gravity waves as well as short Rossby waves are filtered out, and the analysis of moist equatorial Kelvin and long Rossby waves is greatly facilitated.

For low frequency waves, the characteristic time scale (~ 11 days) is smaller than advective time scale ($L/V \approx 29$ days), if the zonal velocity scale V is taken as 4 m s^{-1}. Neglect of nonlinear advection terms is thus a marginally acceptable approximation. We shall consider small perturbation motions about an at-rest basic state.

Based upon observed humidity distributions over the equatorial Indian Ocean (Tomasi 1984), the absolute humidity of the basic state atmosphere is assumed to fall off with height exponentially with a constant water vapor scale height H_1 in the lower troposphere. The mean specific humidity in the layer between pressure p_1 and $p_2(>p_1)$, $\bar{q}(p_1, p_2)$, can then be determined by (Wang 1988a):

$$\bar{q}(p_1, p_2) = q_s \frac{(p_2{}^m - p_1{}^m)}{m(p_2 - p_1)}, \qquad (2.1)$$

where $m = H/H_1$ is the ratio of density scale height H to water vapor scale height, H_1, and q_s is the specific humidity at the surface. On the time scale of a month or so, q_s is well correlated with sea surface temperature (SST) and may be approximated by the following empirical formula (Wang 1988a):

$$q = (0.940 \times \text{SST} (°\text{C}) - 7.64) \times 10^{-3}. \quad (2.2)$$

In order to examine the role of meridional distribution of SST on wave dynamics, the SST in the present model is assumed to be an idealized function of y:

$$\text{SST}(°\text{C}) = \text{SSTM } e^{-\beta y^2/15 C_0} - \frac{\beta y^2}{C_0}, \quad (2.3)$$

where SSTM is the maximum SST at the equator $y = 0$; $C_0 = 50$ m s^{-1} is long gravity wave speed of the gravest baroclinic mode. Numerical values computed using (2.3) are given in Table 1. Also given are observed SST in February along 90°E estimated from Sadler et al. (1987). Between 20°N and 20°S, (2.3) is representative of observed SST profiles over the winter Indian Ocean.

With the foregoing assumptions, basic equations governing low-frequency perturbation motions can be written in pressure coordinates on an equatorial β-plane:

$$\frac{\partial u}{\partial t} - \beta y v = -\frac{\partial \phi}{\partial x}, \qquad (2.4a)$$

$$\beta y u = -\frac{\partial \phi}{\partial y}, \qquad (2.4b)$$

$$\frac{\partial u}{\partial x} + \frac{\partial v}{\partial y} + \frac{\partial \omega}{\partial p} = 0, \qquad (2.4c)$$

$$\frac{\partial}{\partial t}\frac{\partial \phi}{\partial p} + S(p)\omega = -\mu \frac{\partial \phi}{\partial p} - \frac{R}{C_p p} Q_c(p), \quad (2.4d)$$

$$\frac{\partial}{\partial t} M'_v + \frac{1}{g} \int_{p_u}^{p_s} \nabla \cdot (q\mathbf{V}) dp = E'_v - P'_r. \quad (2.4e)$$

The horizontal momentum equations (2.4a, b) and continuity equation (2.4c) are written in conventional forms under semigeostrophic approximation. In the thermodynamic equation (2.4d), only two major diabatic heating processes are included—condensational latent heat and longwave radiation. Here μ denotes a constant coefficient for Newtonian cooling, Q_c expresses condensational heating rate per unit mass, $S(p)$ is static stability parameter, and R and C_p are the gas constant of the air and the specific heat at constant pressure, respectively. In the moisture conservation

TABLE 1. Meridional distributions of SST (°C) computed from (2.3) and observed SST in February over the Indian Ocean (90°E). Observed values are obtained from Sadler et al. (1987).

	Latitude				
	20°S	10°S	0°	10°N	20°N
SST computed from (2.3)	23.6	28.3	30.0	28.3	23.6
Observed SST in Indian Ocean (90°E, February)	25.5	28.0	28.5	27.5	25.0

equation (2.4e), M'_v represents total moisture per unit area (expressed as a depth of liquid water), E'_v and P'_r are the perturbation, evaporation, and precipitation rates, respectively; V represents horizontal wind, p_u and p_s are pressures at the upper boundary and the surface, respectively. It is assumed in deriving (2.4e) that in the equilibrium basic state, evaporation just balances precipitation and the precipitable water of the basic state in the unit area does not change with time.

Since E'_v associated with intraseasonal waves is generally an order of magnitude smaller than P'_r (Wang 1988b), we shall neglect E'_r in the following analysis. Gill (1982) argued that in a "wet" region of moisture convergence the extra moisture gained by convergence is lost as precipitation, whereas in a "dry" region of subsaturation or divergence there is no precipitation and change of moisture content is balanced by moisture divergence. The perturbation precipitation rate is thus related to the rate of moisture convergence in a nonlinear fashion. In this study, we do not attempt to address the effect of the nonlinear heating. Assume the rate of local moisture change small, Eq. (2.4e) reduces to

$$P' = -\frac{b}{g} \int_{p_u}^{p_s} \nabla \cdot (q\mathbf{v}) dp, \qquad (2.5a)$$

where b is a moisture factor that accounts for the fraction of total moisture convergence which condenses out as precipitation. Finally, the condensation heating rate $Q_c(p)$ in (2.4d) can be related to the precipitation rate in the region. The appropriate equation is

$$L_c P'_r = \frac{1}{g} \int_{p_u}^{p_s} Q_c(p) dp, \qquad (2.5b)$$

where L_c is the latent heat. Equations (2.4a–d) and (2.5a, b) consist of a close set of equations if the vertical distribution of heating is specified. The above derivation leads to a heating formulation identical to that of CISK-model which does not treat moisture process explicitly.

3. The 2½ layer model

The behavior of viscous Kelvin wave–CISK modes in a vertically continuous model was discussed in detail by Wang and Chen (1989). Their results suggest that, although an ideal model should consist of more than four levels in the vertical because the lowest four internal modes may have significant response to heat forcing, the basic mechanisms can be qualitatively demonstrated in terms of a simple 2½ layer model which consists of a two-level representation of "free" atmosphere and a well mixed boundary layer. To concentrate on the coupling mechanism between moist Kelvin and Rossby waves and to facilitate analysis, we adopt this low vertical resolution model.

a. Model equations

A schematic structure of 2½ layer model used in Wang (1988a) is given in Fig. 1. Writing horizontal momentum and continuity equations at upper level P_1 and low level P_3 and the thermodynamic equation at midlevel P_2 of the model free atmosphere, expressing vertical derivatives by centered difference of resolution $\Delta p = p_3 - p_1$, and then introducing barotropic and baroclinic parts of wind and geopotential defined by

$$u_+ = \frac{1}{2}(u_3 + u_1), \quad v_+ = \frac{1}{2}(v_3 + v_1),$$

$$\phi_+ = \frac{1}{2}(\phi_3 + \phi_1), \qquad (3.1a)$$

$$u_- = \frac{1}{2}(u_3 - u_1), \quad v_- = \frac{1}{2}(v_3 - v_1),$$

$$\phi_- = \frac{1}{2}(\phi_3 - \phi_1), \qquad (3.1b)$$

we obtain:

$$\frac{\partial u_-}{\partial t} - \beta y v_- = -\frac{\partial \phi_-}{\partial x}, \qquad (3.2a)$$

$$\beta y u_- = -\frac{\partial \phi_-}{\partial y}, \qquad (3.2b)$$

$$\left(\frac{\partial}{\partial t} + \mu\right)\phi_- + C_0^2\left(\frac{\partial u_-}{\partial x} + \frac{\partial v_-}{\partial y}\right)$$
$$= -\frac{R\Delta p}{2C_p p_2} Q_2 - \frac{C_0^2}{2\Delta p}(\omega_e + \omega_u) \qquad (3.2c)$$

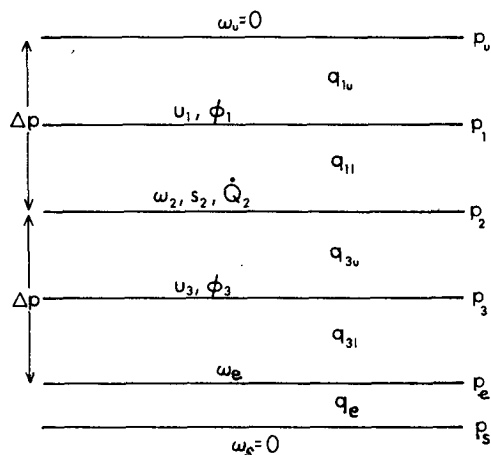$$\frac{\partial u_+}{\partial t} - \beta y v_+ = -\frac{\partial \phi_+}{\partial x}, \qquad (3.2d)$$

FIG. 1. Schematic vertical structure of the model.

$$\beta y u_+ = -\frac{\partial \phi_+}{\partial y}, \tag{3.2e}$$

$$\frac{\partial u_+}{\partial x} + \frac{\partial v_+}{\partial y} + \frac{1}{2\Delta p}(\omega_e - \omega_u) = 0. \tag{3.2f}$$

In Eqs. (3.1) and (3.2), subscripts $+$ and $-$ denote, respectively, the barotropic part for which the velocity is independent of height and the baroclinic part for which the upper level flow is equal and opposite to the low level flow; subscripts 1, 2, and 3 represent variables at pressure levels p_1, p_2, and p_3, respectively; quantities ω_u, ω_2 and ω_e are the vertical pressure velocities at p_u, p_2, and p_e, respectively; Q_2 is condensational heating rate at p_2;

$$C_0 \equiv (S_2 \Delta p^2 / 2)^{1/2}, \tag{3.3}$$

is a constant long gravity wave speed of the gravest baroclinic mode, and S_2 is static stability parameter at p_2. From vertical difference forms of (2.5a, b), Q_2 is expressed as

$$Q_2 = -\frac{bL_c}{\Delta p}[\omega_2(\bar{q}_3 - \bar{q}_1) + \omega_e(\bar{q}_e - \bar{q}_3)], \tag{3.4}$$

where q_e, q_3, and q_1 represent mean specific humidities in the layer (p_s, p_e), (p_e, p_2), and (p_2, p_u), respectively, where (p_i, p_j) denotes the layer between p_i and p_j. In the present model, $p_e = 900$ mb, $p_u = 100$ mb and $p_2 = 500$ mb, q_1 is taken as a constant value of 0.0004, while q_3 and q_e are computed using (2.1).

Using the horizontal velocity scale C_0, the length scale $(C_0/\beta)^{1/2}$, the time scale $(\beta C_0)^{-1/2}$, the geopotential scale C_0^2, and the vertical p-velocity scale $2\Delta p(\beta C_0)^{1/2}$ we obtain nondimensional equations from (3.2) with the aid of (3.4):

$$\frac{\partial u_-}{\partial t} - y v_- = -\frac{\partial \phi_-}{\partial x}, \tag{3.5a}$$

$$y u_- = -\frac{\partial \phi_-}{\partial y}, \tag{3.5b}$$

$$\left(\frac{\partial}{\partial t} + N\right)\phi_- + (1 - I)\left(\frac{\partial u_-}{\partial x} + \frac{\partial v_-}{\partial y}\right)$$
$$= \omega_e(B - 1) + \omega_u(I - 1), \tag{3.5c}$$

$$\frac{\partial u_+}{\partial t} - y v_+ = -\frac{\partial \phi_+}{\partial x}, \tag{3.5d}$$

$$y u_+ = -\frac{\partial \phi_+}{\partial y}, \tag{3.5e}$$

$$\omega_e - \omega_u = -\left(\frac{\partial u_+}{\partial x} + \frac{\partial v_+}{\partial y}\right). \tag{3.5f}$$

The vertical p-velocity at p_2 is

$$\omega_2 = \frac{1}{2}\omega_e + \frac{1}{2}\left(\frac{\partial u_-}{\partial x} + \frac{\partial v_-}{\partial y}\right). \tag{3.6}$$

In (3.5a–f) the nondimensional numbers are

$$N = \mu / \sqrt{\beta C_0} \tag{3.7a}$$

$$I = L_c(\bar{q}_3 - \bar{q}_1)/S \tag{3.7b}$$

$$B = L_c(2\bar{q}_e - \bar{q}_3 - \bar{q}_1)/S \tag{3.7c}$$

$$S = 2C_p p_2 C_0^2/(Rb\Delta p) = (C_p p_2 \Delta p/Rb)S_2, \tag{3.7d}$$

where N is a nondimensional Newtonian cooling coefficient; S measures mean static stability of the basic state; I and B represent ratios of latent heating to adiabatic cooling due to vertical motion at p_2 and p_e, respectively.

b. Boundary layer friction-induced vertical motion

The linear steady barotropic boundary-layer model of Wang (1988a) is employed to evaluate ω_e; details can be found therein. The nondimensional vertical velocity at the top of the boundary layer, p_e, can be expressed in terms of geopotential at p_e, ϕ_e (Wang and Chen 1989):

$$\omega_e = \frac{(p_s - p_e)}{2\Delta p(E^2 + y^2)}\left[\frac{2y}{E^2 + y^2}\left(E\frac{\partial}{\partial y} - y\frac{\partial}{\partial x}\right)\right.$$
$$\left. - E\left(\frac{\partial^2}{\partial x^2} + \frac{\partial^2}{\partial y^2}\right) + \frac{\partial}{\partial x}\right]\phi_e. \tag{3.8}$$

In (3.8), the Ekman number

$$E = \frac{p_e g A_z}{(p_s - p_e)\sqrt{\beta C_0} h \ln(h/z_0)}, \tag{3.9}$$

where A_z is turbulent viscosity, p_e the density at p_e, h the depth of the surface layer, z_0 the surface roughness length, and ln denotes the natural logarithm.

If the characteristic horizontal velocity scales U and V are the same order in the boundary layer while $L_x \gg L_y$, the rhs terms in (3.8) containing differentials with respect to zonal coordinate are higher-order small quantities compared to the remaining terms. To be consistent with the semigeostrophic approximation, the vertical p-velocity at p_e may be simplified as

$$\omega_e = \frac{(p_s - p_e)E}{2\Delta p(E^2 + y^2)}\left(\frac{2y}{E^2 + y^2}\frac{\partial}{\partial y} - \frac{\partial^2}{\partial y^2}\right)(\phi_+ + \phi_-). \tag{3.10}$$

In (3.10), ϕ_e was approximated by $\phi_3 = \phi_+ + \phi_-$. Numerical computations show that (3.10) is a very good approximation to (3.8).

c. Models A and B

If the "rigid lid" upper boundary condition

$$\omega_u = 0, \quad \text{at} \quad p = p_u \tag{3.11}$$

is used, the horizontal divergence of barotropic part is sustained by compression of air columns due to fric-

tional mass convergence [see (3.5f)]. On the other hand, frictional convergence also affects the baroclinic part via adiabatic cooling (heating) and latent heating associated with the boundary-layer frictional moisture convergence [see (3.5c)]. Since boundary layer convergence is controlled by both the baroclinic and barotropic parts, the two parts are coupled through frictional effects. We refer to this model as Model A.

To construct a model in which interactive heating forces only the baroclinic mode, one may replace the rigid lid by a free surface and assume a linearized upper boundary condition:

$$\omega_u = \omega_e, \quad \text{at} \quad p = p_u. \qquad (3.12)$$

It follows from (3.5f) that, (3.12) renders the barotropic part nondivergent. The generation of barotropic part via frictional mass convergence is then artificially eliminated. This allows us to examine an idealized model in which the baroclinic part is independent of the barotropic part. Governing equations for the baroclinic mode only reduce to

$$\frac{\partial u_-}{\partial t} - yv_- = -\frac{\partial \phi_-}{\partial x}, \qquad (3.13a)$$

$$yu_- = -\frac{\partial \phi_-}{\partial y}, \qquad (3.13b)$$

$$\left(\frac{\partial}{\partial t} + N\right)\phi_- + (1 - I)\left(\frac{\partial u_-}{\partial x} + \frac{\partial v_-}{\partial y}\right)$$
$$= \omega_e(B + I - 2), \qquad (3.13c)$$

where ω_e is given by (3.10) with $\phi_+ \equiv 0$. The vertical p-velocity at p_2 is

$$\omega_2 = \omega_e + \frac{1}{2}\left(\frac{\partial u_-}{\partial x} + \frac{\partial v_-}{\partial y}\right). \qquad (3.14)$$

This model is referred to as Model B.

d. The energy equation for Model B

From Eqs. (3.13a–c), the following energy equations are obtained:

$$\frac{\partial}{\partial t}\bar{K} = \langle \bar{p} \cdot \bar{K} \rangle, \qquad (3.15a)$$

$$\frac{\partial}{\partial t}\bar{P} = -(1 - I)\langle \bar{P} \cdot \bar{K} \rangle + GP - N\phi_-^2, \qquad (3.15b)$$

where

$$\bar{K} \equiv \left(\overline{\frac{u_-^2}{2}}\right), \qquad (3.16a)$$

$$\bar{P} \equiv \left(\overline{\frac{\phi_-^2}{2}}\right), \qquad (3.16b)$$

$$\langle \bar{P} \cdot \bar{K} \rangle \equiv \overline{\phi_-\left(\frac{\partial u_-}{\partial x} + \frac{\partial v_-}{\partial y}\right)}, \qquad (3.16c)$$

$$GP \equiv \overline{\omega_e \phi_-}(B + I - 2), \qquad (3.16d)$$

and the "−" notation denotes horizontal average. To the lowest order, kinetic energy K is made of zonal wind component only. This results from the semi-geostrophic approximation. Here $\langle \bar{p} \cdot \bar{K} \rangle$ represents the conversion of available potential to kinetic energy for large scale motion, and GP denotes the generation of wave available potential energy due to the latent heating associated with the boundary-layer moisture convergence; $-N^2\phi_-$ is the potential energy dissipation due to Newtonian cooling. The available potential energy generation due to the latent heating associated with interior wave divergent motion is given by $I\langle \bar{P} \cdot \bar{K} \rangle$. The total generation of available potential energy due to condensational heating is the sum of GP and $I\langle \bar{P} \cdot \bar{K} \rangle$.

4. Moist mode analysis

In Matsuno's (1966) theoretical model, the approximate lateral boundary condition, consonant with β-plane approximation is that ϕ, u and v vanish as y approaches infinity. For numerical computation of the eigenvalue problem we shall assume:

$$\phi_+, \phi_- = 0 \quad \text{at} \quad y = \pm y_0, \qquad (4.1a)$$

where latitudinal circles $y = \pm y_0$ are lateral boundaries. An alternative lateral boundary condition can be proposed as

$$v_+ = v_- = 0 \quad \text{at} \quad y = \pm y_0, \qquad (4.1b)$$

implying that there is no meridional wind crossing the boundaries between the midlatitude westerly regime and the tropical easterly regime. When y_0 is adequately large (about four times the Rossby radius of deformation), the equatorial Kelvin mode and the $m = 1$ and 2 Rossby modes (m is the index of meridional modes) are not affected appreciably by the value of y_0. Numerical computations indicate that the solutions are not sensitive to the forms of lateral boundary conditions. That is to say, use of (4.1a) or (4.1b) yields nearly the same results as long as y_0 is adequately large.

For Model A, solutions to (3.5a–f) with vertical boundary conditions (3.10) and (3.11) are sought of the form:

$$(u_+, v_+, \phi_+, u_-, v_-, \phi_-, \omega_e)$$
$$= R_e[U_+(y)V_+(y), \Phi_+(y), U_-(y), V_-(y),$$
$$\Phi_-(y), \Omega_e(y)]e^{i(kx-\sigma t)} \qquad (4.2)$$

where zonal wavenumber k is given and the complex frequency $\sigma = \sigma_r + i\sigma_r$ is an eigenvalue to be deter-

mined. Complex meridional structure functions $\Phi_+(y)$ and $\Phi_-(y)$ satisfy:

$$(L_1 - L_2)\Phi_+ - L_2\Phi_- = 0, \qquad (4.3a)$$

$$[(N - i\sigma) - (1 - I)L_1 - (B - 1)L_2]\Phi_-$$
$$- (B - 1)L_2\Phi_+ = 0, \quad (4.3b)$$

where

$$L_1 \equiv -\frac{i\sigma}{y^2}\frac{d^2}{dy^2} + \frac{2i\sigma}{y^3}\frac{d}{dy} + \frac{ik}{y^2}, \qquad (4.4a)$$

$$L_2 \equiv -\frac{p_s - p_e}{2\Delta p}\frac{E^2}{E^2 + y^2}\left(\frac{d^2}{dy^2} - \frac{2y}{E^2 + y^2}\frac{d}{dy}\right). \qquad (4.4b)$$

Equation (4.3) with meridional boundary condition (4.1a) are solved for the eigenvalue σ and eigenfunctions Φ_- and Φ_+. Other dependent variables are obtained by

$$U_- = -\frac{1}{y}\frac{d\Phi_-}{dy}, \qquad (4.5a)$$

$$V_- = \frac{ik}{y}\Phi_- + \frac{i\sigma}{y^2}\frac{d\Phi_-}{dy}, \qquad (4.5b)$$

$$U_+ = -\frac{1}{y}\frac{d\Phi_+}{dy}, \qquad (4.5c)$$

$$V_+ = \frac{ik}{y}\Phi_+ + \frac{i\sigma}{y^2}\frac{d\Phi_+}{dy}, \qquad (4.5d)$$

$$\Omega_e = L_2(\Phi_+ + \Phi_-). \qquad (4.5e)$$

For Model B, substituting normal mode solution of the baroclinic component of (4.2) into (3.13a–c) and (3.10) and eliminating U_-, V_-, and Ω_e yield:

$$[(N - i\sigma) - (1 - I)L_1$$
$$- (B + I - 2)L_2]\Phi_- = 0. \quad (4.6)$$

Other fields, U_-, V_-, and Ω_e are given by (4.5a), (4.5b), and (4.5e) with $\Phi_+ \equiv 0$, respectively.

Methods used to solve eigenvalue problems for Models A and B include a finite difference method and a shooting method (Langer 1960). In the absence of heating and dissipation, both methods with $y_0 = 3$ can recover known analytical solutions for Kelvin and Rossby waves with low meridional indices.

A major difficulty encountered in the moist mode analysis is that numerical solutions are sensitive to the width of the equatorial β-plane "channel," $2y_0$, and meridional resolution, Δy. To obtain accurate solutions, one must use adequate values for y_0 and Δy. For the purpose of the present study, it is sufficient to focus on the moist Kelvin and $m = 1, 2$ Rossby modes, which are tightly trapped near the equator.

Comprehensive sensitivity tests have been carried out to assure the convergence of numerical solutions using adequate channel width and meridional resolution. We first examined the depenence of solutions on half-width y_0 using high resolution Δy. For moist Kelvin modes, which turn out to be most unstable, the solutions were found not to change once nondimensional y_0 exceeds two. For moist $m = 1$ Rossby mode, a greater value for y_0 is required to obtain convergent solutions. Figure 2 shows the growth rate $kc_i = \sigma_i$ and phase speed $c_r = \sigma_r/k$ computed using Model B for
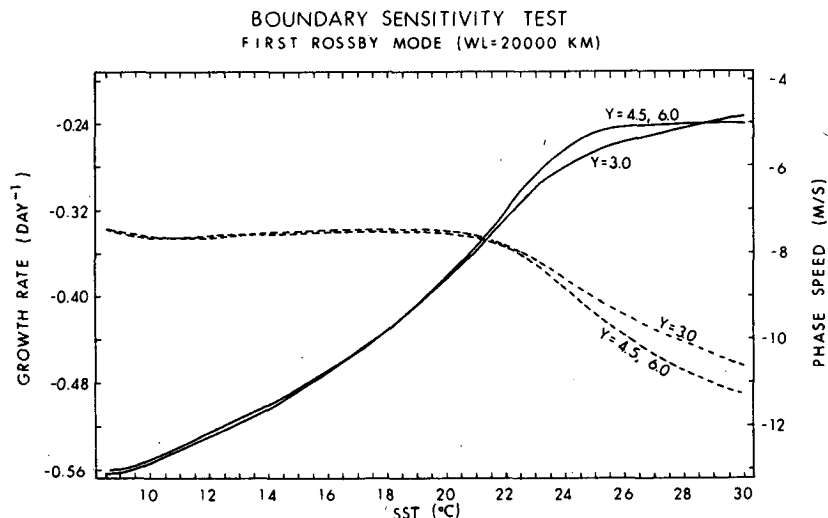

FIG. 2. Values of growth rate (dashed lines) and phase speed (solid lines) computed for the first Rossby mode ($m = 1$) of wavenumber two by shooting method for different half-width of the equatorial β-plane channel, y_0. Nondimensional resolution Δy used in computation is 0.01 (about 0.13 deg lat). The curves for $y_0 = 4.5$ and $y_0 = 6.0$ coincide exactly.

different y_0. When y_0 exceeds about 4.5, solutions for $m = 1$ Rossby mode are nearly the same. These conclusions are valid for all wavelength and SSTM lower than 30°C.

The next examination was the sensitivity of solutions to meridional resolution Δy. For both shooting and finite difference methods, when nondimensional meridional increment $\Delta y < 0.02$ (dimensional Δy_* = 0.27° lat), solutions were found not to change with increasing resolution. We thus use $\Delta y = 0.01$ in shooting method and finite difference method for Model B. For Model A, since finite difference method requires a large memory when the resolution is high, we use Δy = 0.025, corresponding to $N = 241$ if $y_0 = 3$, where N is the number of internal grid points uniformly spaced in the meridional direction. Figure 3 compares the growth rates and phase speeds of the most unstable mode at SSTM = 29°C computed using different resolution N. Solutions display convergence as N increases. The two solutions for $N = 201$ and 241 have maximum errors less than 9%. It is seen that insufficient meridional resolution may cause large computational errors.

In order to check for correct numerical convergence, we also compared results obtained by the finite difference method with those obtained via the shooting method. For adequate values of y_0 and Δy as suggested above both methods yield nearly the same results. The general agreement between the two methods suggest correct convergence and add confidence to the accuracies of the results.

5. Mode selection

a. Inviscid problem

Without boundary layer friction, the baroclinic mode decouples with the barotropic mode and individually satisfies versions of the shallow water equation (3.13a–c). For convenience we rewrite (3.13a–c) as

$$\frac{\partial u_-}{\partial t} - \frac{1}{2} y v_- = - \frac{\partial \phi_-}{\partial x}, \qquad (5.1a)$$

$$\frac{1}{2} y u_- = - \frac{\partial \phi_-}{\partial y}, \qquad (5.1b)$$

$$\frac{\partial \phi_-}{\partial t} \pm \left(\frac{\partial u_-}{\partial x} + \frac{\partial v_-}{\partial y} \right) = 0. \qquad (5.1c)$$

In (5.1) the thermal damping was neglected ($N = 0$); the horizontal velocity, horizontal length, time, and geopotential height were rescaled by $\sqrt{|1 - I|}$ $\times C_0(\sqrt{|1 - I|} C_0/2\beta)^{1/2}$, $(2\beta C_0 \sqrt{|1 - I|})^{-1/2}$, and $|1 - I| C_0^2$, respectively. The positive sign in (5.1c) is taken when $I < 1$, while the negative sign should be used if $I > 1$.

Equation (5.1a–c) allows normal mode solutions of the form

$$(u_-, v_-, \phi_-) = R_e(U, V, \Phi) e^{ik(x-ct)}. \qquad (5.2)$$

Let us first examine Kelvin wave by letting $v_- = 0$ in (5.1). If $I < 1$, equatorially trapped neutral wave exists. In dimensional form, we have

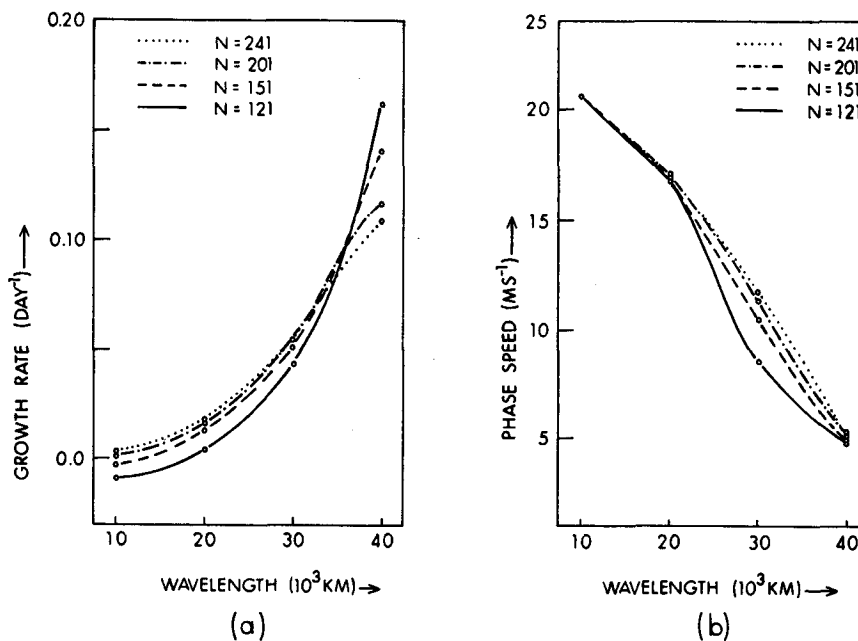(a)   (b)

FIG. 3. (a) Growth rate and (b) phase speed of the most unstable mode in Model A computed using finite difference method for different resolutions. $N = 241$ corresponds to nondimensional resolution $\Delta y = 0.025$ or roughly 0.34 degree of latitude.

$$\Phi(y) = \Phi_0 e^{-\beta y^2/2c} = cU(y), \qquad (5.3a)$$

$$c = C_0\sqrt{1 - I}. \qquad (5.3b)$$

On the other hand, if $I > 1$, no equatorially trapped wave is possible because substituting (5.1a) into (5.1c) leads to

$$c = \pm iC_0\sqrt{I - 1}. \qquad (5.4)$$

Since c is purely imaginary, the eigenfunction (5.3a) does not satisfy the Matsuno-type (1966) boundary condition: $\Phi \to 0$, as $y \to \pm\infty$. The untrapped structure is neither consonant with the equatorial β-plane approximation nor with observations.

For Rossby waves, using (5.2) and eliminating U and Φ yield:

$$\frac{d^2V}{dy^2} - \left(\frac{y^2}{4} + a\right) = 0, \quad I < 1 \qquad (5.5a)$$

$$\frac{d^2V}{dy^2} + \left(\frac{y^2}{4} - a\right) = 0, \quad I > 1 \qquad (5.5b)$$

where

$$a = \frac{1}{2c} \qquad (5.5c)$$

and the boundary condition is

$$V \to 0, \quad \text{as} \quad y \to \pm\infty. \qquad (5.6)$$

For $I < 1$, the general solution can be written as (Abramowitz and Stegan 1972):

$$V(y) = A_1V_1(y) + A_2V_2(y) \qquad (5.7)$$

where

$$V_1(y) = e^{-y^2/4}\left\{1 + \left(a + \frac{1}{2}\right)\frac{y^2}{2!}\right.$$

$$\left. + \left(a + \frac{1}{2}\right)\left(a + \frac{5}{2}\right)\frac{y^2}{4!} + \cdots\right\} \qquad (5.7a)$$

$$V_2(y) = e^{-y^2/4}\left\{y + \left(a + \frac{3}{2}\right)\frac{y^3}{3!}\right.$$

$$\left. + \left(a + \frac{3}{2}\right)\left(a + \frac{7}{2}\right)\frac{y^5}{5!} + \cdots\right\} \qquad (5.7b)$$

are symmetric and asymmetric modes, respectively. To satisfy boundary condition (5.6), parameter a must take the values—$(2m + 1)/2$, where $m = 1, 2, 3, \cdots$*. This leads to a dimensional phase speed:

$$c = -\frac{C_0\sqrt{1 - I}}{2m + 1}, \quad m = 1, 2, 3 \cdots. \qquad (5.8)$$

---

* $m = 0$ gives $c = -1$ which should be rejected because $c + 1 \neq 0$ assumed in deriving (5.5a, b).

These moist long Rossby waves are nondispersive and have an equatorially trapped meridional structure. However, if $I > 1$, the even and odd solutions of (5.5b) are given by (5.7a, b) with $-ia$ written for a and $ye^{i\pi/4}$ for y. In this case, values $a = (2m + 1)/2i$ or $c = -iC_0\sqrt{I - 1}/(2m + 1)$, $(m = 1, 2, 3 \cdots)$ are no longer meaningful eigenvalues which make eigenfunctions satisfy the boundary condition (5.6). When boundary condition at finite y_0, (4.1b), is used, numerical solutions indicate that the eigenvalues vary with the width of the equatorial β-plane channel and the eigenmodes are neutral.

Condition $I < 1$ means that the latent heating rate is smaller than the adiabatic cooling rate due to rising motion in the midlevel of the model. In this stable regime, eastward propagating neutral Kelvin waves and westward propagating neutral Rossby waves coexist, both with reduced phase speeds due to the heating-induced reduction of static stability. When $I > 1$, no equatorially trapped stationary unstable modes are possible. This implies that a single vertical-mode model cannot demonstrate Kelvin–Rossby wave–CISK.

Unless otherwise explained, the values for physical parameters used in the present model are listed in Table 2. Based on typical values for S, H, and H_1 in Table 2, nondimensional number I was calculated as function of SST using (2.1) and (3.7b). Results are shown in Table 3. Typical tropical atmosphere falls in the stable regime $I < 1$. We shall confine our discussion to this regime.

b. Viscous problem

The frictional convergence in the boundary layer is not in phase with the vertical motion at midlevel. When the boundary-layer moisture concentration is sufficiently high, the positive contribution to wave growth due to latent heating induced by frictional moisture convergence will exceed its dissipative contribution. The frictional moisture convergence thus provides additional energy source to destabilize the basic state and realize instability.

TABLE 2. Values for physical parameters used in the models.

Symbol	Parameter	Value
S_2	Static stability parameter	3.14×10^{-6} m^2 s^{-2} p$_a^{-2}$
C_0	Long gravity wave speed of the gravest baroclinic mode	50.1 m s^{-1}
H	Density scale height	7.6 km
H_1	Water vapor scale height	2.2 km
μ	Newtonian cooling coefficient	6×10^{-6} s^{-1}
A_z	Boundary layer turbulent viscosity	10 m^2 s^{-1}
h	Depth of the surface layer	40 m
z_0	Surface roughness	0.01 m
b	Fractional moisture converted into rainfall	0.9

TABLE 3. Values of moisture content and related nondimensional numbers used in the model as functions of SST. The meanings of nondimensional numbers are referred to in the text.

	SST (°C)				
	20.2	24.0	26.0	28.0	30.0
q_s (g kg^{-1})	11.4	14.9	16.8	18.7	20.6
$\bar{q}_e$ (g kg^{-1})	10.1	13.2	14.9	16.5	18.2
$\bar{q}_3$ (g kg^{-1})	5.0	6.5	7.3	8.2	9.0
I	0.47	0.63	0.71	0.80	0.88
$B + I - 2$	0.0	0.63	0.94	1.30	1.65

Figure 4 depicts the phase speed and growth rate varying with SST for moist Kelvin mode and the first and second Rossby modes. Calculations are for the gravest baroclinic mode in Model B. At SSTM = 8.2°C, there is no moisture below 500 mb, so that the values represent those for dry modes. Boundary layer friction and Newtonian cooling damp these waves and slow their propagation. When SST increases, the propagation speeds for both Kelvin and Rossby modes are reduced but the directions of their movement remain unchanged (Fig. 4a). It is apparent that the reduction of the phase speed is mainly caused by the wave convergence-dependent heating, which results in a smaller effective static stability. In a previous analysis of moist Kelvin waves, one of the authors found that heating due to boundary-layer moisture convergence slightly increases the eastward propagation speed for Kelvin

waves (Wang 1988a). It is of interest to notice the distinct behavior of moist Kelvin and Rossby modes in the growth rate (Fig. 4b); growth rate of the moist Kelvin mode increases with rising SST and amplification occurs as SSTM exceeds a critical value (about 29°C). On the other hand, growth rates of both first and second Rossby modes slightly decrease with rising SST and remain negative at all times. It is clear that the additional energy supply due to boundary-layer frictional moisture convergence favors only the amplification of moist Kelvin waves.

The mode selection in the present model is related to the spatial distribution of frictional moisture convergence, which is an important contributor to the generation of perturbation energy. The rate of generation of perturbation available potential energy due to the latent heating associated with frictional moisture supply is $(B + I - 2)\omega_e\phi_-$ [see Eq. (3.16d)], where the coefficient $(B + I - 2)$ is a function of SST. In the present model it is positive (negative) when SST is greater (less) than 20.2°C; it increases with rising SST as shown in Table 3. Normally, high SST occurs near the equator, implying that the equatorial warm water region is conducive for the generation of wave energy when ω_e and ϕ_- are positively correlated. Figures 5a, b illustrate horizontal distribution of ϕ_- and ω_e computed from Model B for dry Kelvin wave, while Figs. 6a, b illustrate those for dry $m = 1$ Rossby mode. For the Kelvin mode, both ϕ_- and ω_e fields have maximum amplitudes at the equator. They are also almost in

MODE SELECTION (WL=20000 KM)
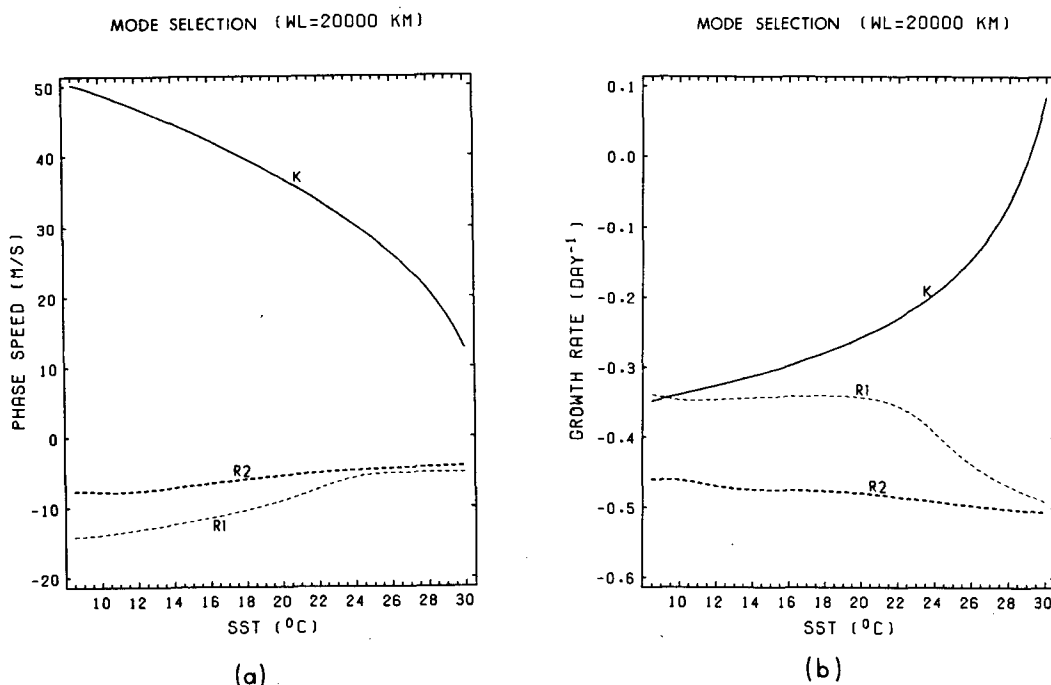
MODE SELECTION (WL=20000 KM)

FIG. 4. (a) Phase speed and (b) growth rate of the moist Kelvin mode (K), $m = 1$ Rossby mode (R1), and $m = 2$ Rossby mode (R2) as functions of SSTM computed from Model B. The wavelength is 20 000 km.
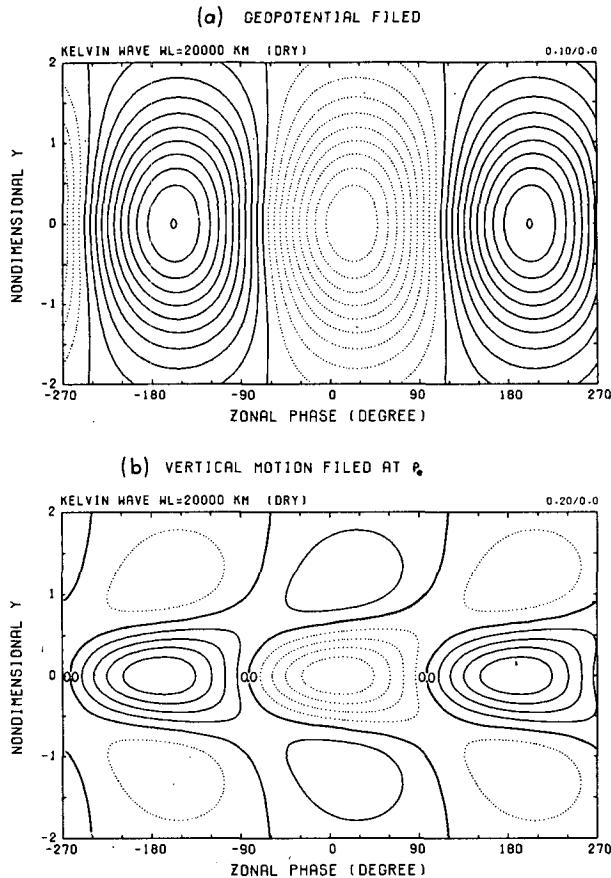
(a) GEOPOTENTIAL FILED

(b) VERTICAL MOTION FILED AT P_s

FIG. 5. Horizontal structures for (a) geopotential thickness, ϕ_- and (b) vertical pressure velocity at the top of the boundary layer, ω_e, computed for a dry damped Kelvin wave in Model B. Solid and dashed lines indicate positive (or zero) and negative contours, respectively; contour intervals for ω_e is 20% of the maximum value and that for ϕ_- is 10% of the maximum value.

phase near the equator. This strong positive covariance implies an efficient generation of eddy available potential energy when the boundary layer moisture content exceeds 10 g kg^{-1} so that $B + I - 2 > 0$ (Table 3). For $m = 1$ Rossby mode, ω_e has maximum at the equator and around $y = \pm 1$. Near the equator between 0.75 and -0.75, ϕ_- and ω_e are negatively correlated. This situation is destructive to wave energy generation when moisture content is high near the equator. Away from the equator near $y = \pm 1$ there are narrow bands where ϕ_- and ω_e are positively correlated. These bands shift poleward as SST increases, and the moisture content within the bands is much lower than that in the equatorial belt. As a result, there is no net generation of wave energy due to frictional moisture convergence-induced latent heating.

6. The impact of the horizontal mode-coupling

To elucidate on the impact of coupling between the moist Kelvin and Rossby modes via boundary-layer

frictional convergence/divergence, we focus again on the single gravest baroclinic mode first. We shall compare results obtained from two models: one is Model B in which Kelvin and Rossby modes coexist; the other is a viscous Kelvin wave–CISK model in which the meridional winds vanish in the model free atmosphere. For the convenience of comparison, SST is assumed to be uniformly distributed in both models. The complex frequency in the viscous Kelvin wave–CISK model was previously obtained (Wang 1988a):

$$\sigma = -\frac{iN}{2} + \left[k^2(1 - I) - \frac{N^2}{4} \right.$$

$$\left. + ik\frac{(p_s - p_e)}{2\Delta pE}(B + I - 2) \right]^{1/2}. \quad (5.1)$$

a. Growth rate and phase speed

Figure 7 compares growth rates and phase speeds computed from (a) Model B (dash-dotted lines), and (b) viscous Kelvin wave–CISK model (dotted lines)

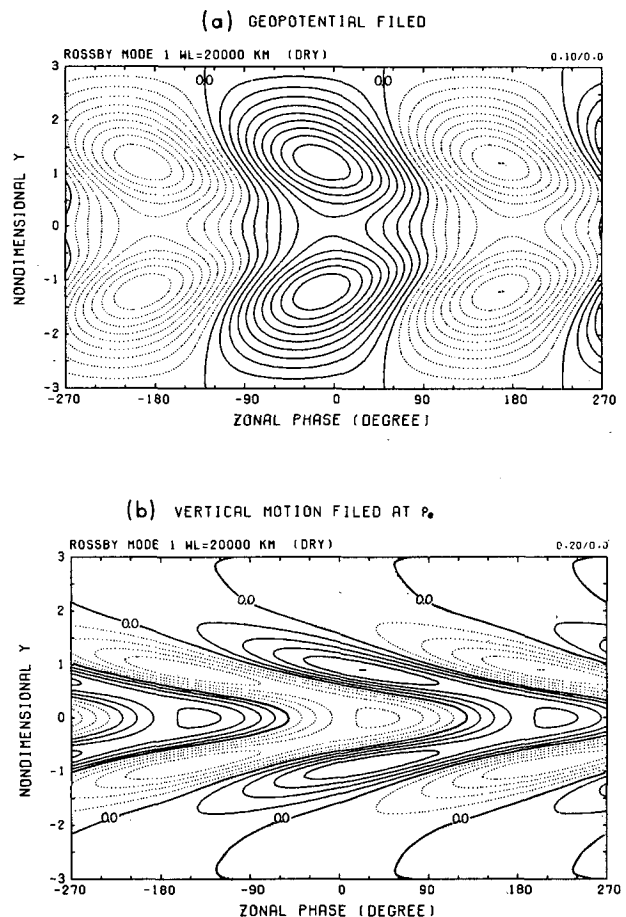(a) GEOPOTENTIAL FILED

(b) VERTICAL MOTION FILED AT P_s

FIG. 6. As in Fig. 4 except for a dry $m = 1$
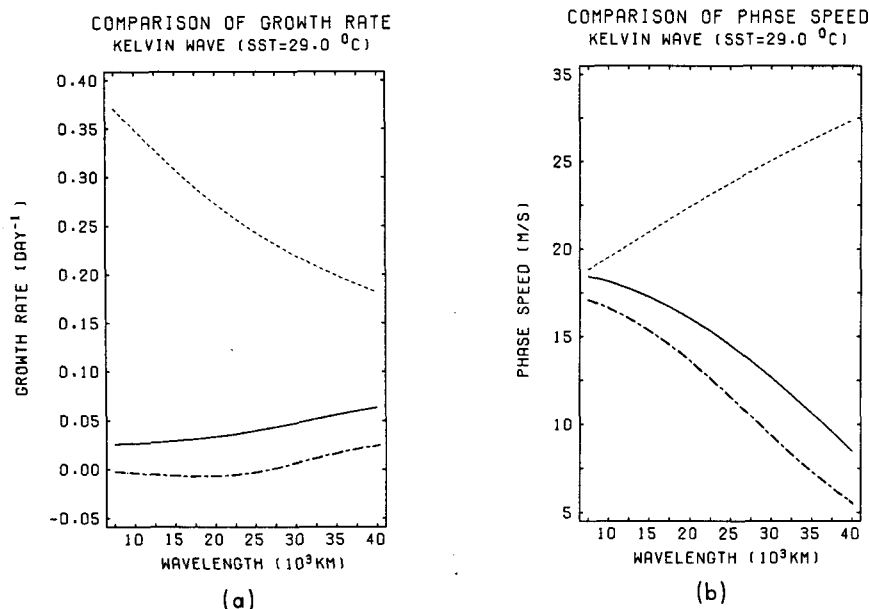Rossby wave in Model B.

FIG. 7. Comparison of (a) growth rate and (b) phase speed as functions of wavelength. Dotted, dash-dotted, and solid lines indicate values computed from Eq. (5.1) of the viscous Kelvin wave–CISK model, the Model B with uniform SST = 29°C, and the Model B with latitude dependent SST (2.3), respectively. All other parameters are the same as listed in Table 2 except $\mu = 5 \times 10^{-6}\,\text{s}^{-1}$.

for uniform SST = 29°C. There are several noticeable differences. First, the phase speed of the pure moist Kelvin mode increases with increasing wavelength and are between 18 and 30 m s^{-1}, whereas the phase speed of the most unstable mode in Model B decreases with increasing wavelength and are between 18 and 6 m s^{-1}. This suggests that the coupling between moist Kelvin and Rossby modes slows the propagation of the moist unstable mode, especially for long waves.

Second, the growth rate of the unstable mode in Model B is substantially smaller than that of the viscous Kelvin wave–CISK mode. Observed development of an intraseasonal OLR anomaly low (which is a measure of deep convection activity) occurs in the equatorial Indian Ocean and western Pacific with a composite rate of intensification about 15 W m^{-2} pentad^{-1}, corresponding to an e-folding time an order of 5 days (Rui and Wang 1990). After crossing the date line where
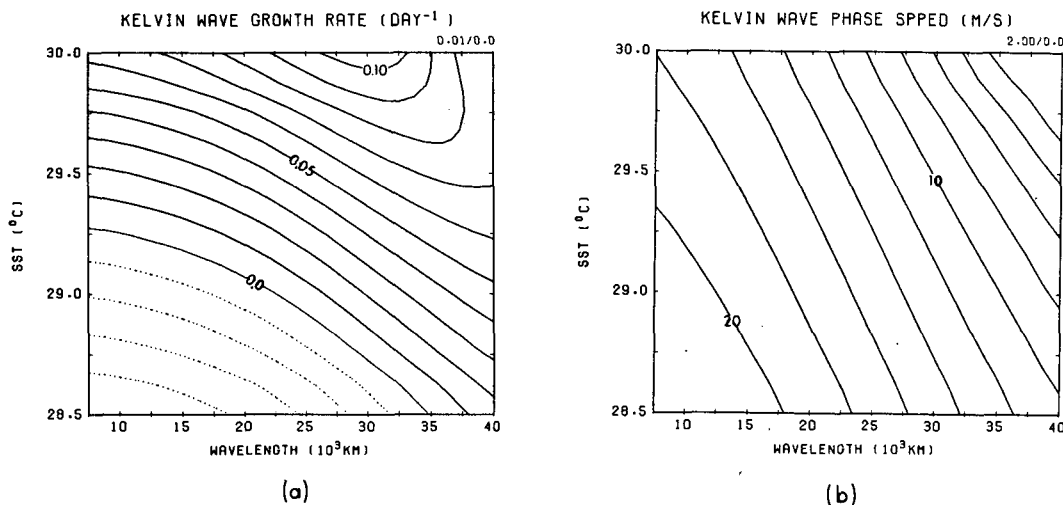

FIG. 8. (a) Growth rate and (b) zonal phase speed of the unstable mode in Model B as functions of wavelength and the maximum SST at the equator.
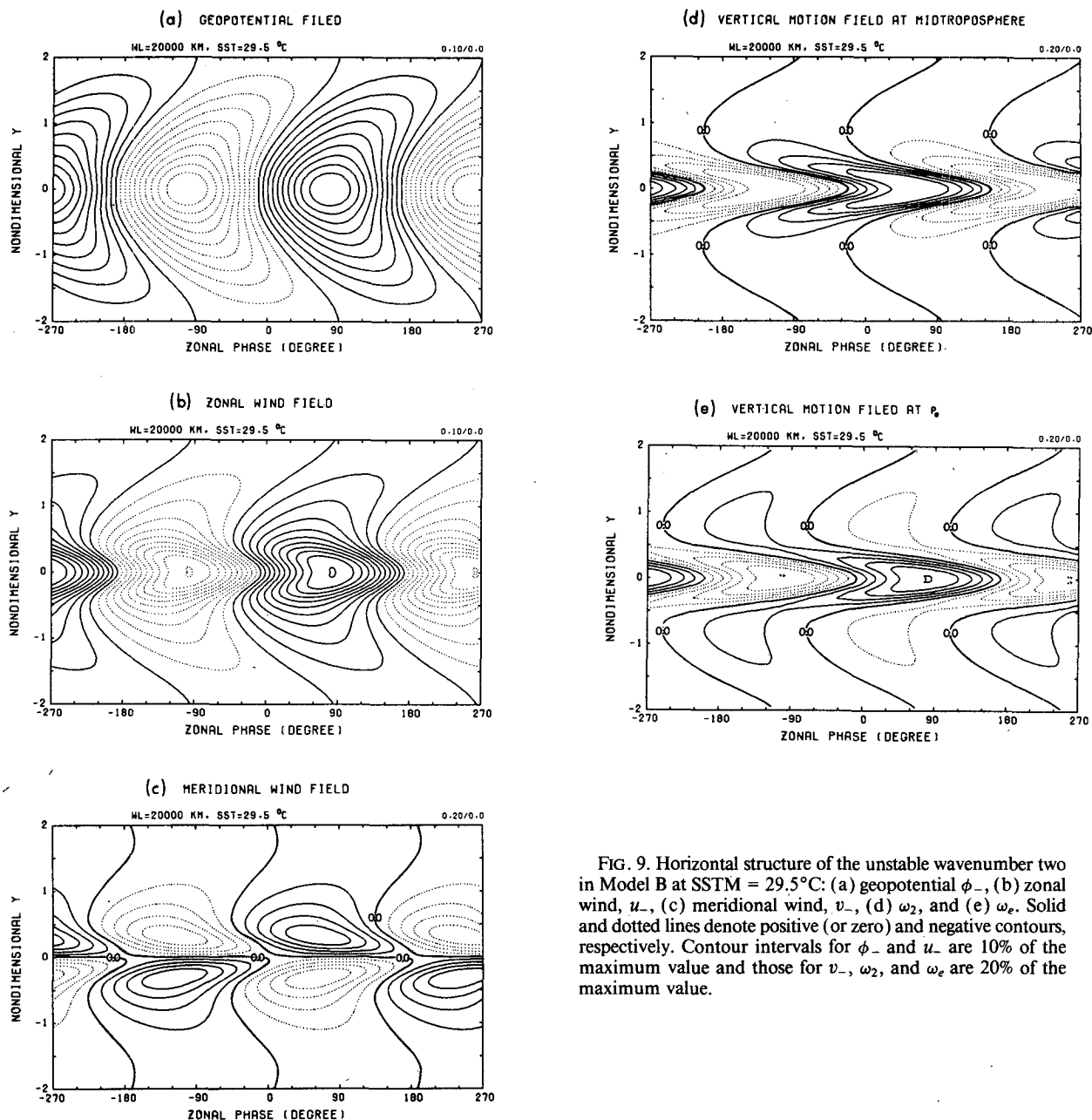
(a) GEOPOTENTIAL FILED

(b) ZONAL WIND FIELD

(c) MERIDIONAL WIND FIELD

(d) VERTICAL MOTION FIELD AT MIDTROPOSPHERE

(e) VERTICAL MOTION FILED AT P_s

FIG. 9. Horizontal structure of the unstable wavenumber two in Model B at SSTM = 29.5°C: (a) geopotential ϕ_-, (b) zonal wind, u_-, (c) meridional wind, v_-, (d) ω_2, and (e) ω_e. Solid and dotted lines denote positive (or zero) and negative contours, respectively. Contour intervals for ϕ_- and u_- are 10% of the maximum value and those for v_-, ω_2, and ω_e are 20% of the maximum value.

SST drops below 27.5°C, the intraseasonal convection anomalies tend to decay rapidly. It seems plausible to consider 28°C as a critical SST for the development of the intraseasonal modes and 5 days as a typical e-folding time scale for growth rate at a maximum SST of 30°C. For a given thermal damping coefficient (5 $\times 10^{-6}$ s^{-1}), the most unstable Kelvin wave–CISK mode grows as SSTM exceeds 25°C, and obtains a large growth rate of 0.5 day^{-1} at SSTM = 30°C, whereas the most unstable mode in coupled Model A amplifies as SSTM exceeds 28.3°C and obtains a moderate growth rate of 0.15 day^{-1}. Comparing these observa-

tions, it is apparent that the growth of the unstable mode in coupled model A or B is more realistic than that of an uncoupled Kelvin–wave CISK mode. In fact, one of the drawbacks of the viscous Kelvin wave–CISK is that strong thermal damping (Newtonian cooling coefficient 15 $\times 10^{-6}$ s^{-1}) is necessary for the purpose of explaining the observed development over a warm ocean surface (SST higher than 28°C, for example) and slow eastward propagation (say, 10–15 m s^{-1}) (Wang and Chen 1989). It was speculated that the large damping rate may crudely account for the horizontal mode coupling effects and nonlinear effects that

(a) GENERATION OF EP DUE TO ω_e

WL=20000 KM. SST=29.5 °C   0.20/0.0

NONDIMENSIONAL Y

ZONAL PHASE (DEGREE)

(b) CONVERSION FROM EP TO EK

WL=20000 KM. SST=29.5 °C   0.20/0.0
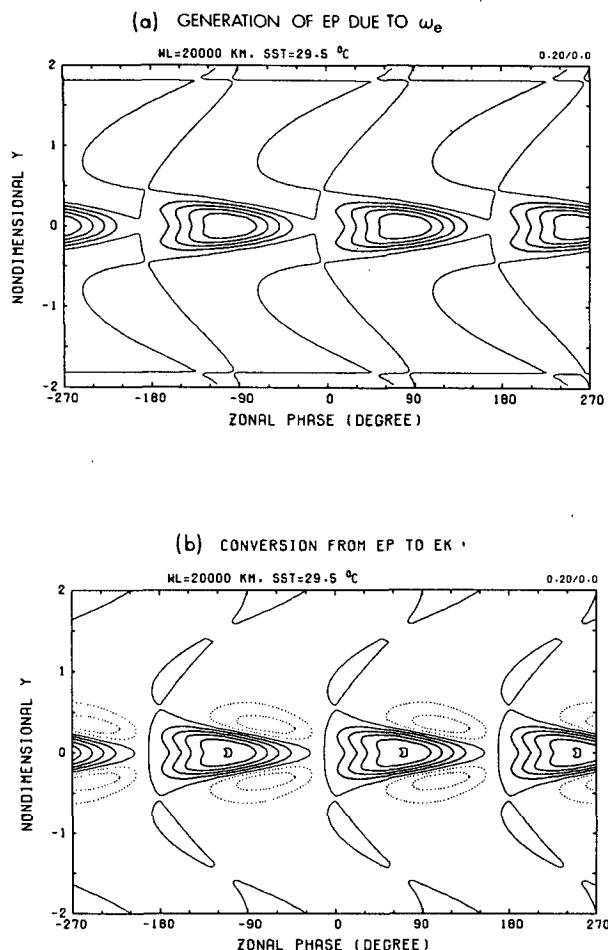
NONDIMENSIONAL Y

ZONAL PHASE (DEGREE)

FIG. 10. Horizontal distribution of the (a) generation of available potential energy due to frictional convergence-induced latent heating, and (b) generation of kinetic energy computed for unstable wavenumber two at SSTM = 29.5°C in Model B. Solid and dotted lines are positive (or zero) and negative contours, respectively. Contour intervals are 20% of the maximum value.

are absent in the model. In the presence of meridional wind components and the coupling between Kelvin and Rossby modes, it indeed requires only a much smaller Newtonian cooling coefficient, 5×10^{-6} s^{-1}, to explain the observed development and slow propagation.

Another important difference is that in the Kelvin wave–CISK model the shortest wave has the largest growth rate while in Model B the longest wave is most unstable. This implies that coupling between Kelvin and Rossby modes favors the development of longest planetary waves. This wavelength selection is an interesting result and deserves further examination. Figure 8 displays the dependences of growth rate and phase speed on the wavelength and SSTM computed from Model B. Figure 8a indicates the longest wave being most unstable until SSTM exceeds 29.5°C. Above this temperature wavelength of the fastest growing wave

gradually shifts to shorter planetary scales (wavenumber 2). The propagation speeds of the most unstable waves are slow, generally less than 10 m s^{-1}. It has been found that the coupling between vertical modes via the boundary-layer frictional effect may result in long-wave selection in the viscous Kelvin wave–CISK model (Wang and Chen 1989). The result here demonstrates that interaction between Kelvin and Rossby modes via the boundary-layer frictional effect displays a similar dynamic effect, leading to a preferred planetary scale of instability.

b. Horizontal structure and energetics

Figures 9a–e show horizontal structure of the moist unstable mode in Model B at SSTM = 29.5°C for wavenumber 2. The geopotential ϕ_- and zonal wind u_- nearly satisfy geostrophic relation. Both of them are symmetric about and trapped near the equator. These properties are similar to those of the moist Kelvin wave. However, unlike the moist Kelvin wave, there exists significant meridional wind component whose amplitude is about one-quarter that of the zonal wind component. Meridional winds are asymmetric about the equator with extrema located at one-half Rossby radius of deformation away from the equator. This feature results from coupling between Kelvin and Rossby modes via boundary layer frictional effect. This coupling is further enhanced by the feedback from latent heating associated with moisture convergence. The vertical motion at midlevel is maintained by interior divergent motion and boundary layer mass convergence/divergence with the former dominating. The horizontal structure suggests that the moist unstable mode in Model B is a Kelvin wave modified by latent heating and by coupling with $m = 1$ Rossby wave via boundary-layer frictional effect.

Figure 10a illustrates horizontal distribution of the generation of wave available potential energy (GP) due to the latent heating caused by boundary-layer moisture convergence for the unstable mode. Maximum occurs in the neighborhood of the extrema of ϕ_- field and tightly trapped near the equator. The wave kinetic energy is also generated near the equator and almost in phase with GP (Fig. 10b). The destruction of kinetic energy occurs on both sides of the equator around $y = \pm 0.4$. This destruction is mainly caused by negative covariance between ϕ_- and $\partial v_-/\partial y$. This suggests that meridional motions consume kinetic energy of the equatorial unstable mode.

c. Comparison of results obtained from the Model A and B

The growth rate and zonal phase speed computed from Models A and B are compared in Fig. 11. Both models yield similar wave selection patterns, but the growth in Model A is significantly larger than that in
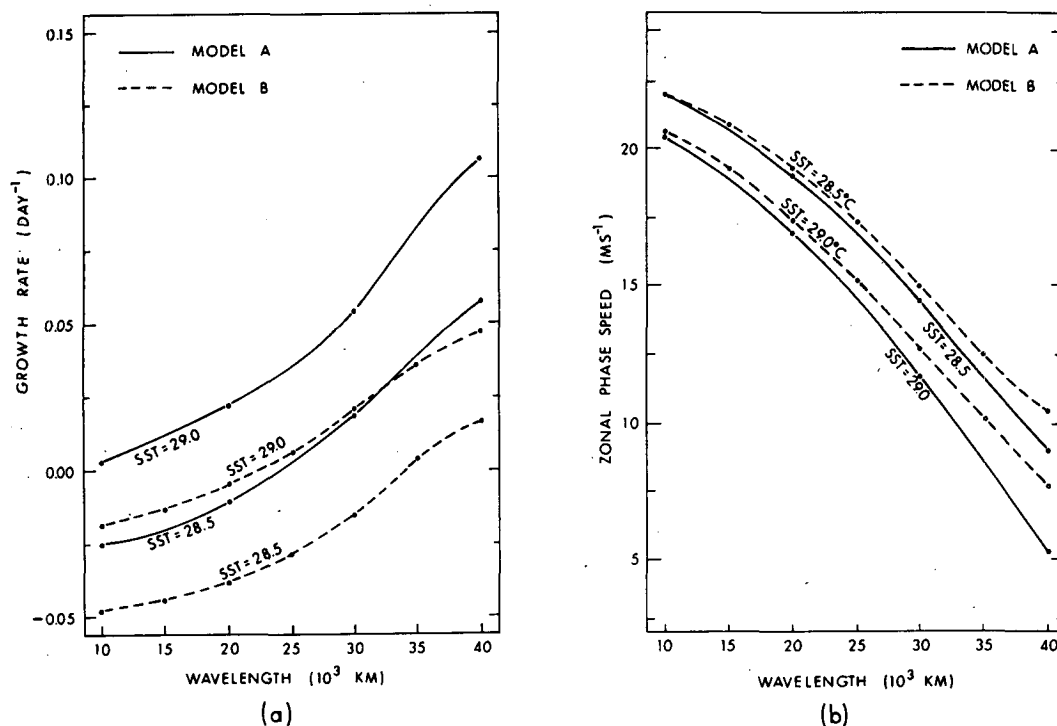
FIG. 11. (a) Growth rate and (b) zonal phase speed of the unstable mode in Model A (solid lines) and Model B (dashed lines) as functions of wavelength at SSTM = 28.5 and 29.0°C. Resolutions Δy used in Models A and B are 0.025 and 0.01, respectively.

Model B for all wavelengths on planetary scales. The eastward propagation in Model A is slower than in Model B, particularly at the long-wave limit. It is apparent that coexistence of the two vertical modes does not change the wave selection resulting from horizontal model coupling. The vertical mode coupling, however, enhances wave growth and reduces propagation speed.

The vertical mode coupling also slightly modifies wave structure. The horizontal structure of the baroclinic component of the unstable mode in Model A (figures are not shown) is extremely similar to that of the single unstable baroclinic mode in Model B. Both resemble a modified Kelvin mode. However, the structure of the barotropic component of the unstable mode in Model A is very different from that of the baroclinic component (Fig. 12). The maximum amplitude of ϕ_+ field is located around $y = \pm 1.5$. The amplitude near the equator is about 40% of the maximum value. The u_+-field is in geostrophic balance with ϕ_+-field and symmetric about the equator, while the v_+-field is antisymmetric about the equator.

It is noticeable that horizontal divergence of the barotropic wind component is forced by the compression associated with frictional upward motion [Eq. (3.5f)]. This implies that the barotropic component could bear structural features of $m = 1$ Rossby mode through the influence of frictional mass convergence. We note also that the maximum amplitude of the

baroclinic component is about five times that of the barotropic component. Since the former has a maximum at the equator while the latter has a maximum off the equator, the amplitude of the baroclinic component near the equator is an order of magnitude greater than that of the barotropic component. The compound flow fields in the equatorial zonal plane are determined, to a large extent, by the baroclinic component. Consequently, upper level flows are nearly out of phase with low level flows, and the nature of instability such as wavelength selection and mode selection in Models A and B are essentially similar to each other.

7. Response of the instability to meridional variation of SST

We first point out that a meridionally varying SST profile (2.3) is more favorable for wave amplification than a uniform SST profile, if the SSTs at the equator are the same. This can be seen from Fig. 6, in which the solid and dash-dotted curves represent results computed using the meridionally varying SST profile (2.3) with SSTM = 29°C and using a uniform SST = 29°C, respectively. This indicates that stronger heating intensity away from the equator does not favor development of equatorially trapped unstable waves.

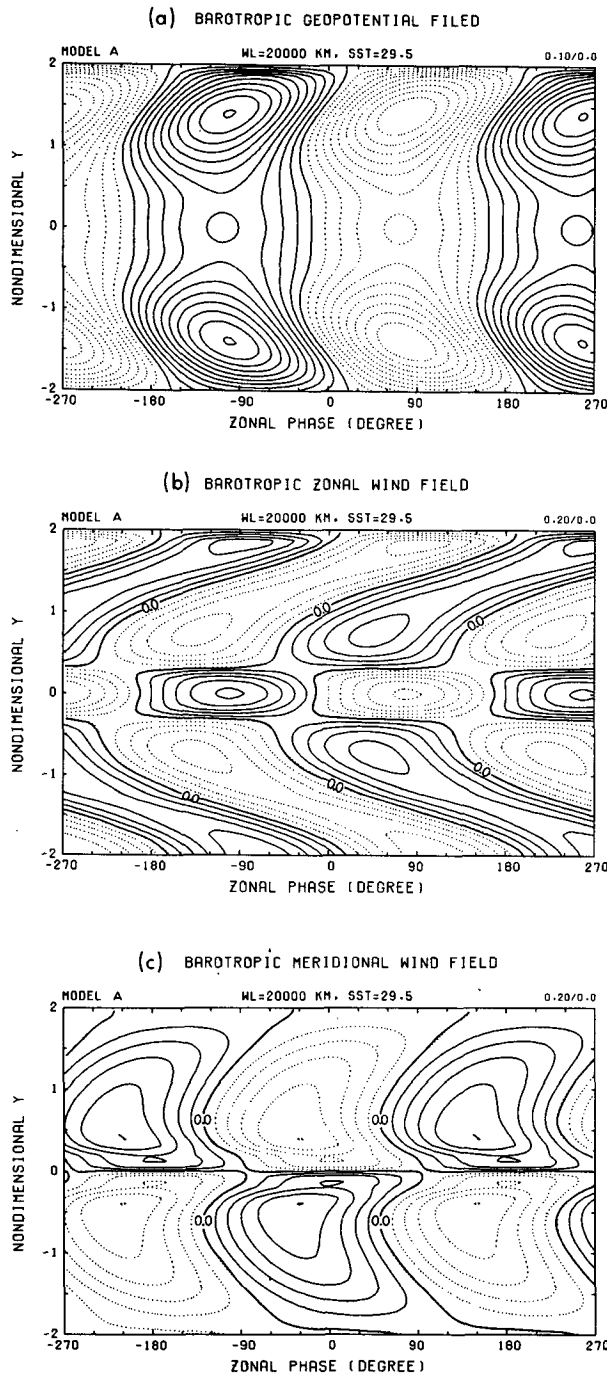Meridional distribution of SST in the tropics exhibits

(a) BAROTROPIC GEOPOTENTIAL FILED

(b) BAROTROPIC ZONAL WIND FIELD

(c) BAROTROPIC MERIDIONAL WIND FIELD

FIG. 12. Horizontal structure of the barotropic component of the unstable wavenumber two in Model A at SSTM = 29.5°C: (a) geopotential ϕ_+, (b) zonal wind u_+, and (c) meridional wind v_+. Solid and dotted lines are positive (or zero) and negative contours, respectively. The interval for ϕ_+ is 10% of the maximum value while that for u_+ and v_+ are 20% of the maximum value.

significant annual variation. In the western Pacific and Indian Ocean region, the maximum zonally averaged SST is located between 5° and 10°N in boreal summer

and moves to 0°–5°S in boreal winter. To simulate the SST distribution in the boreal summer, we assume:

$$SST(y) = SSTM \; e^{-(y-0.5)^2/15} - (y - 0.5)^2 \quad (7.1)$$

where y is nondimensional meridional coordinate scaled by $(\beta C_0)^{1/2}$. The profile (7.1) has the same shape as profile (2.3) but the maximum shifts northward by about 7.5° latitude.

Using the SST profile (7.1) in Model B, we calculated growth rates and phase speeds for the moist modified Kelvin, $m = 1$ and $m = 2$ Rossby modes. Results are plotted in Fig. 13. When SST maximum shifts to 7.5°N, the growth rate of the unstable mode decreases substantially for all wavelength, while the propagation speed increases. It is also noteworthy that both symmetric $m = 1$ and $m = 2$ antisymmetric Rossby modes remain damped.

The horizontal structure of the unstable mode computed using SST profile (7.1) (figure not shown) indicates that due to the northward shift of the maximum SST or available moist static energy of the basic state, the strongest vertical motion at midlevel shifts from the equator to about 3°N, meanwhile, stronger meridional winds also occur north of the equator.

This experiment demonstrates that the amplification of the unstable wave is controlled by the dynamic effect of the geographical equator and the thermodynamic effect of the "thermal equator" where maximum SST occurs. The former tends to constrain the unstable disturbance near the equator because it is of a modified Kelvin wave nature. On the other hand, the SST distribution affects the condensational heating field which contributes to the wave development. When the maximum SST moves away from the equator, decrease in moist static energy source near the equator leads to a decrease in the growth rate of unstable waves. This appears to reasonably explain why the eastward propagation in equatorial region is stronger in boreal winter than in boreal summer.

8. Summary

We have analyzed the behavior of the horizontally coupled unstable mode in a linear, semigeostrophic, 2½ layer, equatorial β-plane model. The present model has augmented the moist Kelvin-wave model by including meridional wind components, boundary layer frictional effects, and latitude-dependent SST or moist static energy for the basic state. It allows investigation of the impacts of horizontal mode coupling and annual march of SST on moist, equatorially trapped low-frequency waves.

Without sufficient moisture supply, the atmosphere is stable. Due to the presence of thermal and boundary layer dissipations, westward moving Rossby waves decay faster than eastward moving Kelvin waves. When moisture concentration gradually increases, the moist Kelvin mode becomes progressively less damped and
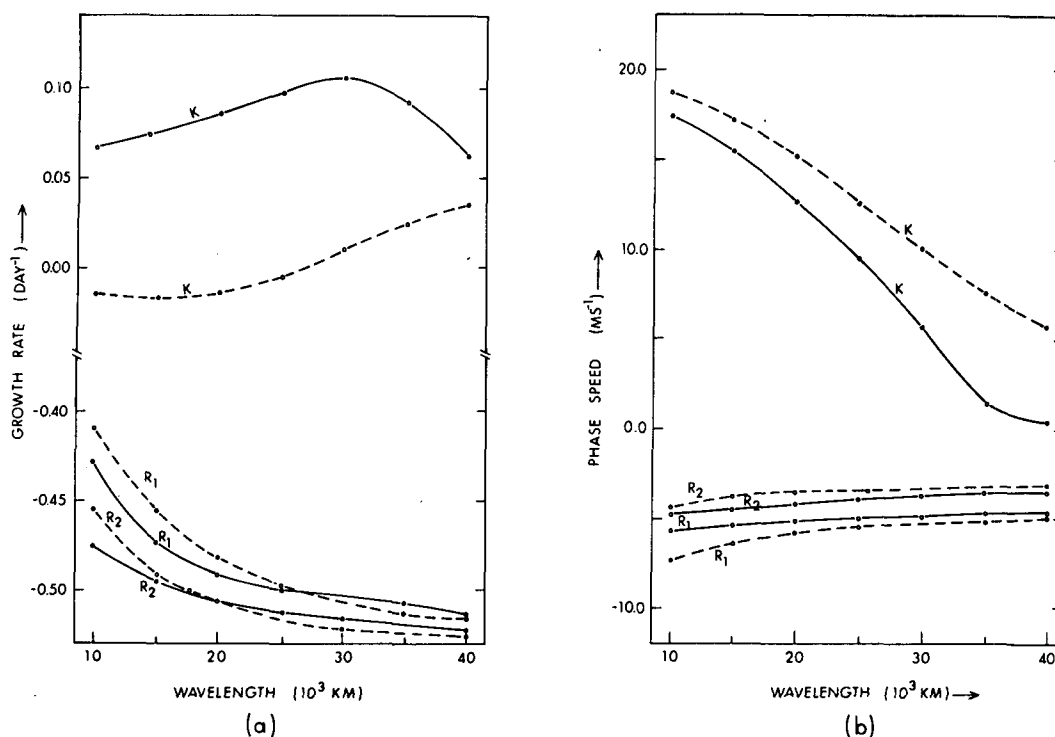
FIG. 13. Comparison of (a) growth rate and (b) zonal phase speed of the unstable mode in Model B computed using SST profile (2.3) (solid lines) and (7.1) (dashed lines). In both cases the maximum SST is 30°C.

finally begins to grow when SST exceeds a critical value. On the other hand, moist Rossby waves are always damped (Fig. 4). The unstable mode selection in the present model can be explained in terms of wave energy generation due to latent heating induced by boundary-layer frictional moisture convergence. Because of the large concentration of moisture in the boundary layer, the latent heating associated with frictional moisture convergence produces a substantial portion (about one-third) of the wave energy. Since the availability of basic-state moist static energy is highest at the equator, the equatorial warm water region is most conducive (or destructive) for wave energy generation. In this region, both Kelvin and Rossby wave-induced boundary layer convergences reach their maxima (Figs. 5 and 6); however, the frictional upward motion is positively correlated with temperature in the Kelvin mode, while the negative covariance between them is found for the Rossby mode. Thus, available potential energy is generated efficiently by the frictional convergence-induced latent heating in the moist Kelvin mode, but is destroyed in the moist Rossby modes.

Although unstable modes appear to be rooted in Kelvin waves, they are modified by the dynamic coupling with Rossby waves. The horizontal structure of the unstable mode resembles that of Kelvin waves but exhibits significant meridional wind components, which are asymmetric about the equator and similar to that of the lowest meridional mode of Rossby wave

(Fig. 9). Another evidence of the coupling is that the barotropic component of the unstable mode has a modified $m = 1$ Rossby wave structure (Fig. 12), although the dominant baroclinic component resembles Kelvin-wave structure. This supports the notion that the unstable mode is a moist coupled Kelvin–Rossby mode.

Coupling between the moist Kelvin mode and the Rossby mode via boundary-layer frictional convergence and associated latent heating has fundamental impacts on wave instability. Horizontal mode coupling acts as an efficient brake on eastward propagation and suppresses unrealistically fast growth of the pure Kelvin wave–CISK mode (Fig. 7). More importantly, it favors the amplification of long planetary waves, rather than short waves, providing a wavelength selection mechanism (Fig. 8a). The vertical mode coupling between the baroclinic and barotropic components further enhances the growth rate and slows zonal propagation of the unstable modes (Fig. 11).

The annual variation of equatorial intraseasonal wave activity is caused by the annual march of the "thermal" equator where the highest SST is located. This notion is confirmed by an experiment in which the maximum SST is shifted to 7.5°N, a situation occurring during boreal summer. In this case, the growth rate of the unstable coupled Kelvin–Rossby mode is substantially reduced (Fig. 13). Separation of the thermal effect of warm ocean water from the dynamic effect

of the equator stabilizes the tropical atmosphere for planetary-scale low frequency disturbances.

An attempt has been made to examine the stability of the tropical atmosphere with respect to the asymmetric equatorial Rossby mode ($m = 2$) when SST distribution is asymmetric about the equator. We found no westward propagating growing mode in association with asymmetric long Rossby modes. The assumption of the semigeostrophic approximation confined our discussion to planetary zonal scales. The question of whether shorter Rossby modes could grow rapidly remains unanswered.

The choice of a parameter value for B and I is consistent with the CISK model formulation. However, as one anonymous reviewer pointed out, the basic-state moist available potential energy in the CISK model may be overestimated by using larger values in B and I. A direct consequence of using a smaller value for $B + I$ is the reduction of instability for other given parameters. This should not be seen as a defect of the model, since a variety of other energy sources are available to excite such motions. More importantly, the Newtonian cooling coefficient used here (6×10^{-6} s^{-1}) is also too large. When a smaller thermal damping is assumed the instability will increase. Therefore, the reduction in growth rate due to reduced $B + I$ can well be compensated by the increase in growth rate caused by reduced thermal damping. The important point here is that the major conclusions regarding 1) mode selection, 2) effects of horizontal mode coupling, and 3) effect of off-equatorial SST maxima are not affected by the choice of particular parameter values.

Observational analyses of horizontal structure of the intraseasonal modes have been carried out by Madden (1986), Knuston et al. (1986), Murakami (1987), and Rui and Wang (1989). Although detailed structures obtained using various datasets or analytical approaches differ to some extent, these studies agree that substantial meridional winds are present off the equator and that the equatorial zonal winds appear to be associated with subtropical rotational cells. Observed meridional wind anomalies on intraseasonal time scales seem to be much stronger than those of unstable modes in the present model. The model also failed to simulate the linkage of equatorial zonal winds and subtropical or midlatitude rotational cells. In the nonlinear single vertical-mode model of Hendon (1988), the unstable mode is reported to have a clear coupling of equatorial zonal winds and subtropical rotational cells (his Fig. 8), suggesting an important nonlinear effect. When wave propagation speed becomes comparable to perturbation wind speed, the nonlinear advective effect is expected to play an important part in the wave dynamics.

REFERENCES

Abramowitz, M., and I. A. Stegan, 1972: *Handbook of Mathematical Functions.* Dover, 1046 pp.
Chang, C.-P., and H. Lim, 1988: Kelvin wave-CISK: A possible mechanism for the 30–50 day oscillations. *J. Atmos. Sci.,* **45,** 1709–1720.
Gill, A. E., 1982: Studies of moisture effects in simple atmospheric model: The stable case. *Geophys. Astrophys. Fluid Dyn.,* **19,** 119–152.
Hayashi, Y. Y., and A. Sumi, 1986: The 30–40 day oscillations simulated in an "Aqua Planet" model. *J. Meteor. Soc. Japan,* **64,** 451–467.
Hendon, H. H., 1988: A simple model of the 40–50 day oscillation. *J. Atmos. Sci.,* **45,** 569–584.
Knutson, T. R., K. M. Weickmann and J. E. Kutzbach, 1986: Global-scale intraseasonal oscillation of outgoing longwave radiation and 200 mb zonal wind during Northern Hemisphere summer. *Mon. Wea. Rev.,* **114,** 605–623.
Langer, R. E., 1960: *Boundary Problems in Differential Equations.* The University of Wisconsin Press, 324 pp.
Lau, K.-M., and L. Peng, 1987: Origin of low frequency (intraseasonal) oscillations in the tropical atmosphere. Part I: The basic theory. *J. Atmos. Sci.,* **44,** 950–972.
——, and S. Shen, 1988: On the dynamics of intraseasonal oscillation and ENSO. *J. Atmos. Sci.,* **45,** 1781–1797.
Lau, N.-C., I. M. Held and J. D. Neelin, 1988: The Madden–Julian oscillation in an idealized GCM model. *J. Atmos. Sci.,* **45,** 3810–3832.
Madden, R. A., 1986: Seasonal variations of the 40–50 day oscillations. *J. Atmos. Sci.,* **43,** 3138–3158.
——, and P. R. Julian, 1972: Description of global-scale circulation cells in the tropics with 40–50 day period. *J. Atmos. Sci.,* **29,** 1109–1123.
Matsuno, T., 1966: Quasi-geostrophic motions in the equatorial area. *J. Meteor. Soc. Japan,* **44,** 25–43.
Murakami, T., 1987: Intraseasonal atmospheric teleconnection patterns during the Northern Hemisphere summer. *Mon. Wea. Rev.,* **115,** 2133–2154.
Neelin, J. D., I. M. Held and K. H. Cook, 1987: Evaporation-wind feedback and low frequency variability in the tropical atmosphere. *J. Atmos. Sci.,* **44,** 2341–2348.
Rui, H., and B. Wang, 1990: Development characteristics and dynamic structures of tropical intraseasonal convection anomalies. *J. Atmos. Sci.,* **47,** 357–379.
Sadler, J. C., M. A. Lander, A. M. Hori and L. K. Oda, 1987: Tropical marine climate atlas. Vols. I and II. UHMET 87-01 and 87-02, Dept. of Meteorology, University of Hawaii.
Swinbank, R., T. N. Palmer and M. K. Davey, 1988: Numerical simulation of the Madden and Julian oscillation. *J. Atmos. Sci.,* **45,** 774–788.
Tomasi, C., 1984: Vertical distribution features of atmospheric vapor in the Mediterranean, Red Sea, and Indian Ocean. *J. Geophys. Res.,* **89,** D2, 2563–2566.
Wang, B., 1988a: Dynamics of tropical low frequency waves: An analysis of moist Kelvin waves. *J. Atmos. Sci.,* **45,** 2051–2065.
——, 1988b: Comments on "An air–sea interaction model of intraseasonal oscillation in the tropics." *J. Atmos. Sci.,* **45,** 3521–3525.
——, and J.-K. Chen, 1989: On the zonal scale selection and vertical structure of the equatorial intraseasonal waves. *Quart. J. Roy. Meteor. Soc.,* **115.**
——, and H. Rui, 1990: Synoptic climatology of transient tropical convection anomalies: 1975–1985. *Meteor. Atmos. Phys.,* in press.
Yamagata, T., 1987: A simple moist model relevant to the origin of intraseasonal disturbances in the tropics. *J. Met. Soc. Japan,* **65,** 153–164.